Gravitational recoil from binary black hole mergers in scalar field clouds

Yu-Peng Zhang,[1] Miguel Gracia-Linares,[2] Pablo Laguna,[2] Deirdre Shoemaker,[2] and Yu-Xiao Liu[1]

[1]*Lanzhou Center for Theoretical Physics, Key Laboratory of Theoretical Physics of Gansu Province,*
Institute of Theoretical Physics, Research Center of Gravitation,
School of Physical Science and Technology, Lanzhou University, Lanzhou 730000, China
[2]*Center of Gravitational Physics, Department of Physics,*
University of Texas at Austin, Austin, Texas 78712, USA

(Received 4 October 2022; accepted 20 January 2023; published 17 February 2023)

In vacuum, the gravitational recoil of the final black hole from the merger of two black holes depends exclusively on the mass ratio and spins of the coalescing black holes, and on the eccentricity of the binary. If matter is present, accretion by the merging black holes may modify significantly their masses and spins, altering both the dynamics of the binary and the gravitational recoil of the remnant black hole. This paper considers such a scenario. We investigate the effects on the kick of the final black hole from immersing the binary in a scalar field cloud. We consider two types of configurations: one with nonspinning and unequal-mass black holes, and a second with equal mass and spinning holes. For both types, we investigate how the gravitational recoil of the final black hole changes as we vary the energy density of the scalar field. We find that the accretion of the scalar field by the merging black holes could have a profound effect. For the nonspinning, unequal-mass binary black holes, the kicks are in general larger than in the vacuum case, with speeds of $\sim 1,200$ km/s for binaries with mass ratio $2:1$, 1 order of magnitude larger than in vacuum. For equal mass, binaries with black holes with spins aligned with the orbital angular momentum, kicks larger than in vacuum are also found. For systems with spins in the superkick configuration, the scalar field triggers a similar dependence of the kicks with the entrance angle at merger as in the vacuum case but in this case depending on the strength of the scalar field.

DOI: 10.1103/PhysRevD.107.044039

I. INTRODUCTION

The gravitational waves (GWs) emitted during the inspiral and coalescence of a binary black hole (BBH) carry energy, angular momentum, and linear momentum [1]. A net loss of linear momentum by the binary in a certain direction implies a recoil of the final black hole (BH) in the opposite direction [2–4]. In vacuum, this recoil or kick depends exclusively on the mass ratio and spins of the coalescing BHs, and if the binary is not in a quasicircular orbit, the recoil depends also on the eccentricity of the binary system [5]. When matter is present, the situation is more complex. For instance, in mixed binary mergers, i.e. coalescences of BHs with neutron stars, the kick will depend also on any accretion of matter by the BH during the merger [6].

For this work, we focus on BH environments permeated by a scalar field. Scalar fields have been considered as sources of dark matter [7], in inflationary theories [8–13], and in the context of modified theories of gravity, such as scalar-tensor and $f(R)$ theories [14–16]. In the presence of BHs, scalar fields have also been used to probe the transition from inspiraling BHs to a single perturbed BH [17]. BBH systems in scalar-tensor [18,19], $f(R)$ [20], and Einstein-Maxwell-dilation [21] theories have been also studied, as well as BBHs in dynamical Chern-Simons gravity [22], axionlike scalar fields [23], and scalar Gauss-Bonnet gravity [24].

Here, we are interested in investigating the effect that a scalar field may have on the kick of the final BH, an aspect not considered by the studies mentioned above. We focus on a simple scenario, a BBH immersed in a spherical shell of a massive scalar field and study two types of BBH configurations. One consists of unequal mass binaries with nonspinning BHs, and in the other, binaries with equal-mass holes but spinning BHs. For the later, we consider BH spins aligned with the orbital angular momentum (i.e., nonprecessing binaries) and BH spins in the orbital plane in the superkick configuration [25,26]. In addition to the kick on the final BH, we also studied the characteristics of the GWs and the angular momentum radiated in GWs and by the scalar field.

The paper is organized as follows. In Sec. II, we present the method to construct initial data. Section III summarizes the equations of motion for the BBH with scalar field sources. Section IV presents the methodology to extract kicks, energy, and angular momentum radiated. The BBH configurations are given in Sec. V. Results for unequal mass, nonspinning BHs binaries are given in Sec. VI and for equal mass, spinning BHs binaries in Sec. VII. Conclusions are found in Sec. VIII. Greek indices denote space-time indices, and Latin indices are used for spatial indices. We use geometrical units in which $G = c = 1$. A subscript 0 denotes initial values. Unless explicitly stated, we report results in units of M_0, the total initial mass of the BBH system.

II. INITIAL DATA

Under a $3+1$ decomposition of the Einstein field equations [27], the initial data consist of $(\gamma_{ij}, K_{ij}, \rho, S_i)$, with γ_{ij} the spatial metric and K_{ij} the extrinsic curvature of the constant time, spacelike hypersurfaces. ρ and S_i are the energy and momentum densities, respectively. The initial data must satisfy the following equations:

$$R + K^2 - K_{ij}K^{ij} = 16\pi\rho \tag{1}$$

$$\nabla_j K^j_i - \nabla_i K = 8\pi S_i, \tag{2}$$

namely the Hamiltonian and momentum constraints, respectively. Here R is the Ricci scalar, and ∇ denotes covariant differentiation associated with γ_{ij}. For our case of a massive scalar field,

$$\rho = \frac{1}{2}\Pi^2 + \frac{1}{2}\nabla^i\nabla_i\phi + \frac{1}{2}m_\phi^2\phi^2, \tag{3}$$

$$S_i = -\Pi\partial_i\phi, \tag{4}$$

with m_ϕ the mass of the scalar field ϕ and Π its conjugate momentum.

We solve the constraints (1) and (2) following the York-Lichnerowicz conformal approach [28–31] in which

$$\gamma_{ij} = \psi^4\eta_{ij} \tag{5}$$

$$K_{ij} = A_{ij} = \psi^{-2}\tilde{A}_{ij}, \tag{6}$$

with ${A^i}_i = 0$, $K = 0$, and η_{ij} the flat metric. In addition, we impose $\phi = \tilde{\phi}$ and $\Pi = \psi^{-6}\tilde{\Pi}$ [32,33]. With these transformations, the Hamiltonian (1) and the momentum (2) constraints read respectively:

$$\Delta\psi + \frac{1}{8}\tilde{A}^{ij}\tilde{A}_{ij}\psi^{-7} = -\pi\tilde{\Pi}^2\psi^{-7} - \pi\psi\partial^i\phi\partial_i\phi - \pi m_\phi^2\phi^2\psi^5 \tag{7}$$

$$\partial_j\tilde{A}^j_i = -8\pi\tilde{\Pi}\partial_i\phi, \tag{8}$$

where $\Delta = \eta^{ij}\partial_i\partial_j$.

Since we are modeling BHs as punctures, the conformal factor ψ diverges at the punctures. Therefore, we will exploit the freedom for choosing initial data for ϕ and Π and zero out the divergent terms proportional to ψ and ψ^5 in Eq. (7). We accomplish this by setting initially $\phi = 0$. With this assumption, (7) and (8) become

$$\Delta\psi + \left(\frac{1}{8}\tilde{A}^{ij}\tilde{A}_{ij} + \pi\tilde{\Pi}^2\right)\psi^{-7} = 0 \tag{9}$$

$$\partial_j\tilde{A}^j_i = 0, \tag{10}$$

respectively.

In Eq. (8), we use the Bowen-York solutions for $\tilde{A}_{ij}$, where the initial binary configuration is fully specified by the mass, spin, and momenta of the BHs, and their separation. These parameters are obtained from integrating the post-Newtonian (PN) equations of motion. The integration starts at large separations and ends at the separation where the numerical relativity (NR) initial data are constructed. This method is known to yield initial data suitable for stitching together NR and PN evolutions [34]. Since we are interested in asymptotically flat solutions to the conformal factor, we require $\tilde{\Pi}$ to have compact support. For simplicity, we set

$$\tilde{\Pi}(r) = \Pi_0 \exp\left[-\frac{1}{2}\left(\frac{r - r_0}{\sigma}\right)^2\right]. \tag{11}$$

That is, the scalar field source is a shell with radius r_0, thickness σ, and amplitude Π_0. We solve Eq. (9) with the 2Punctures solver [35], which was modified to include the $\tilde{\Pi}^2$ term.

III. EVOLUTION EQUATIONS

The evolution equation for the scalar field is

$$\Box\phi = m_\phi^2\phi, \tag{12}$$

with $\Box = \nabla^\mu\nabla_\mu$ and ∇_μ covariant differentiation with respect to the space-time metric $g_{\mu\nu}$. Under a $3+1$ decomposition, the space-time metric is decomposed as

$$g_{\mu\nu} = \gamma_{\mu\nu} - n_\mu n_\nu, \tag{13}$$

with $n^\mu = (\alpha^{-1}, -\beta^i\alpha^{-1})$ the timelike unit normal vector to the $t =$ constant spacelike hypersurfaces. Here α and β^i are the lapse function and shift vector, respectively. Given (13), we rewrite Eq. (12) as

$$\frac{1}{\alpha}\partial_o\phi = -\Pi, \tag{14}$$

$$\frac{1}{\alpha}\partial_o\Pi = -\nabla^i\nabla_i\phi - \nabla_i \ln\alpha\nabla^i\phi + K\Pi + m_\phi^2\phi, \tag{15}$$

where $\partial_o = \partial_t - \beta^i\partial_i$.

The evolution of the geometry of the spacelike hypersufaces, namely γ_{ij} and K_{ij}, is handled with the Baumgarte

Shapiro Shibata Nakamura formulation of the Einstein equations [36,37]. For a scalar field, the stress-energy tensor source in these equations is given by

$$S_{ij} = \nabla_i\phi\nabla_j\phi + \frac{1}{2}\gamma_{ij}(\Pi^2 - \nabla^k\nabla_k\phi - m_\phi^2\phi^2). \tag{16}$$

We used the moving puncture gauge [38,39] to evolve α and β^i. The resulting set of evolution equations is solved numerically using the Maya code [40–45], our local version of the Einstein Toolkit code [46].

IV. PHYSICS EXTRACTION

The physical quantities of interest are the spin and masses of the BHs, as well as the properties of the radiated emission. The BH masses and spins are computed using the dynamical apparent horizons framework [47] as implemented in the Einstein Toolkit[46]. On the other hand, the energy, linear and angular momentum radiated are computed from the Weyl scalar Ψ_4 as follows [1]:

$$\frac{dE^{\mathrm{gw}}}{dt} = \lim_{r\to\infty}\frac{r^2}{16\pi}\oint\left|\int_{-\infty}^{t}\Psi_4 dt'\right|^2 d\Omega, \tag{17}$$

$$\frac{dP_i^{\mathrm{gw}}}{dt} = \lim_{r\to\infty}\frac{r^2}{16\pi}\oint \hat{l}_i\left|\int_{-\infty}^{t}\Psi_4 dt'\right|^2 d\Omega, \tag{18}$$

$$\frac{dJ_i^{\mathrm{gw}}}{dt} = -\lim_{r\to\infty}\frac{r^2}{16\pi}\mathrm{Re}\left[\oint\left(\int_{-\infty}^{t}\bar{\Psi}_4 dt'\right)\times \hat{J}_i\left(\int_{-\infty}^{t}\int_{-\infty}^{t'}\Psi_4 dt'' dt'\right)d\Omega\right], \tag{19}$$

where $d\Omega = \sin\theta d\theta d\varphi$, $\hat{l}_i = (\sin\theta\cos\varphi, \sin\theta\sin\varphi, \cos\theta)$, and $\hat{J}_i$ is the angular momentum operator. Integration of (18) yields the recoil or kick of the final BH from the emission of GWs.

In addition to GW emission, we also have emission of energy, linear, and angular momentum associated with the scalar field. We compute this emission following the method in Ref. [24] as follows:

$$\frac{dE^{\mathrm{sf}}}{dt} = \lim_{r\to\infty} r^2\oint T_{tr} d\Omega, \tag{20}$$

$$\frac{dP_i^{\mathrm{sf}}}{dt} = \lim_{r\to\infty} r^2\oint T_{ir} d\Omega, \tag{21}$$

$$\frac{dJ_z^{\mathrm{sf}}}{dt} = \lim_{r\to\infty} r^2\oint T_{\phi r} d\Omega, \tag{22}$$

where the components of the stress-energy tensor are given by

$$T_{\mu\nu} = \nabla_\mu\phi\nabla_\nu\phi - g_{\mu\nu}\left(\frac{1}{2}\nabla_\alpha\phi\nabla^\alpha\phi + \frac{1}{2}m_\phi^2\phi^2\right). \tag{23}$$

In all these fluxes, we evaluate the integrals at a finite radius and then extrapolate the values to infinity.

V. BINARY CONFIGURATIONS AND CONVERGENCE TEST

The initial configuration for all BBH systems has the holes separated by a coordinate distance $d = 8M_0$. The scalar field momentum shell has radius $r_0 = 12M_0$ and thickness $\sigma = 1M_0$. We also set the mass of the scalar field to $m_\phi = 0.4/M_0$. Each simulation was carried out with eight levels of mesh refinements, outer boundary at $317.44M_0$, and resolution in the finest grid of $M_0/64.5$.

We considered two types of binaries. One is binaries with nonspinning BHs and initial mass ratios $q_0 = m_1/m_2 = (2, 3, 4)$. The other type is binaries with equal mass BHs and their spins antialigned spins with magnitudes $a = 0.6$. For the spinning cases, we investigated two

TABLE I. ADM and scalar field energies in the initial data for unequal mass, nonspinning BBH configurations.

Case	E_ϕ/M_0	E_{ADM}/M_0
q2-000	0.0000	0.989
q2-050	0.0289	1.018
q2-075	0.0643	1.053
q2-100	0.1126	1.102
q3-000	0.0000	0.991
q3-050	0.2889	1.019
q3-075	0.0643	1.055
q3-100	0.1126	1.104
q4-000	0.0000	0.992
q4-050	0.2889	1.021
q4-075	0.0643	1.056
q4-100	0.1126	1.105

TABLE II. ADM and scalar field energies in the initial data for equal mass, spinning BBH configurations.

Case	E_ϕ/M_0	E_{ADM}/M_0
$a_\parallel$000	0.0000	0.987
$a_\parallel$050	0.0289	1.016
$a_\parallel$075	0.0643	1.052
$a_\parallel$100	0.1127	1.101
$a_\perp$0000	0.0000	0.987
$a_\perp$0125	0.0018	0.989
$a_\perp$0250	0.0072	0.995
$a_\perp$0375	0.0163	1.004
$a_\perp$0500	0.0289	1.017
$a_\perp$0625	0.0449	1.033
$a_\perp$0750	0.0643	1.052
$a_\perp$0875	0.0869	1.075
$a_\perp$1000	0.1127	1.101

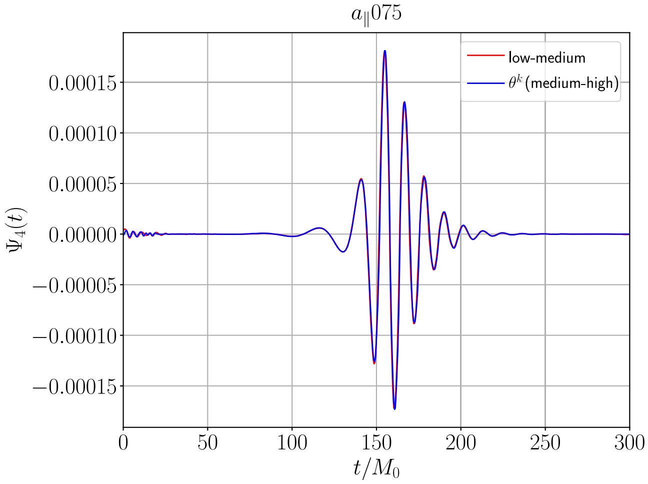

FIG. 1. Convergence test: plots of the (2, 2) mode of the Weyl scalar Ψ_4 extracted at $r = 75M$ for the differences (low–medium), superposed with θ^k (medium–high). θ is the resolution factor, in this case $\theta = 1.5$, and k is the convergence rate. We obtain a convergence rate of $k = 1.8$.

setups: one with the BH spins aligned with the orbital momentum (nonprecessing binaries) and spins in the orbital plane (superkick configuration). With the exception of the superkick configuration binaries, we considered initial amplitude values of the scalar momentum $\hat{\Pi}_0 \equiv \Pi_0 M_0 \times 10^3 = (5.0, 7.5, 10.0)$. On the other hand, for superkick binaries, we have added more cases and set $\hat{\Pi}_0 = (1.25, 2.5, 3.75, 5.0, 6.25, 7.5, 8.50, 10.0)$. In order to do comparisons with the vacuum case, we did simulations with $\hat{\Pi}_0 = 0$ for all types. The labeling of the simulations is as follows: A nonspinning, $q_0 = \mathrm{x}$ with $\hat{\Pi}_0 = \mathrm{y.y}$ simulation is labeled qx-0yy. Similarly, an equal mass simulation with spins perpendicular and parallel to the orbital angular momentum with the same $\hat{\Pi}_0$ are labeled $a_{\perp}$0yy and $a_{\|}$0yy, respectively.

Tables I and II show the scalar field energies E_{ϕ} and total ADM energy E_{ADM} in the initial data for each of the cases. Notice that $E_{\mathrm{ADM}} \simeq E_{\mathrm{ADM}}^{\mathrm{vac}} + E_{\phi}$ where [48]

$$E_{\phi} = \int \rho\sqrt{\gamma} d^3x = \frac{1}{2}\int \tilde{\Pi}^2 \psi^{-6} \sqrt{\eta} d^3x. \tag{24}$$

To check the convergence of our numerical results, we performed a series of three simulations with low, medium and high resolutions, $M_0/43$, $M_0/64.5$, and $M_0/95.75$, respectively at the finest mesh. The binary parameters are those corresponding to the case $a_{\|}075$. Figure 1 shows plots of the (2, 2) mode of the Weyl scalar Ψ_4 extracted at $r = 75M$ for the differences (low–medium), superposed with θ^k (medium–high). θ is the resolution factor, in this case $\theta = 1.5$, and k is the convergence rate. From the superposition, we obtain a convergence rate $k = 1.8$, which is acceptable for the results in the present study.

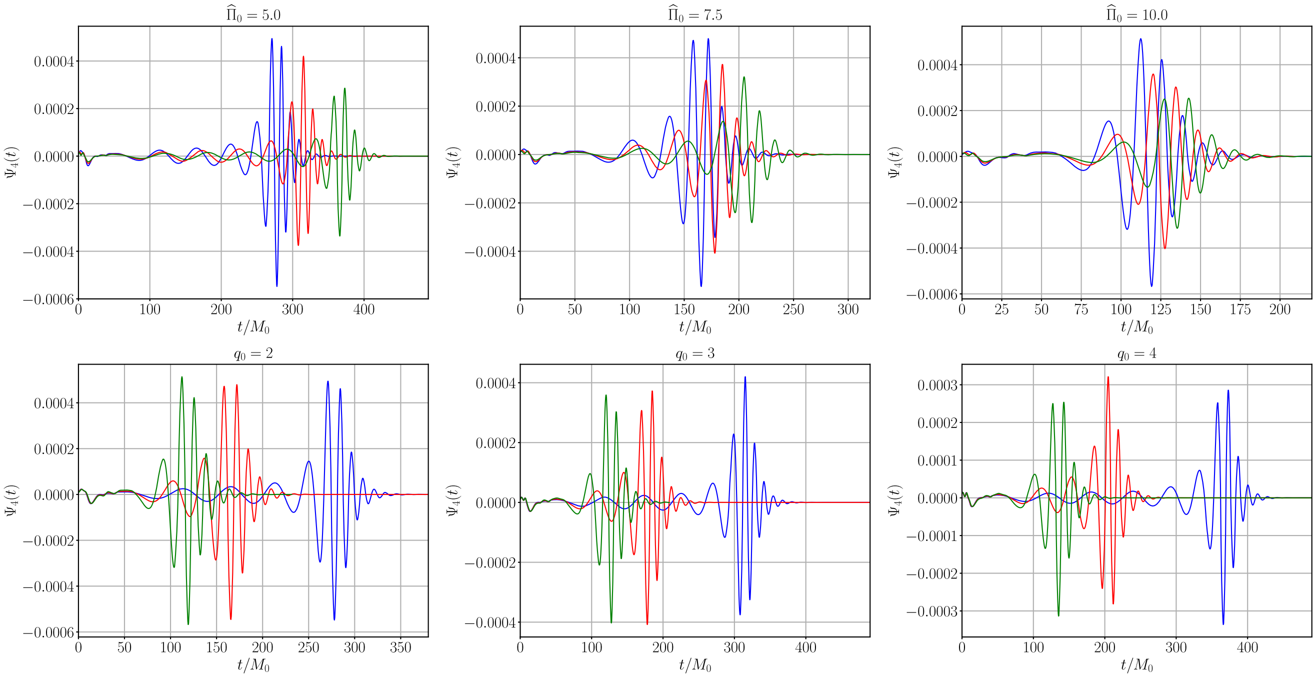

FIG. 2. Mode $l = 2$, $m = 2$ of the Weyl scalar Ψ_4 for the unequal mass and nonspinning BH binaries. The top panels from left to right are for $\hat{\Pi}_0 = (5.0, 7.5, 10.0)$, respectively, with lines blue, red, and green corresponding to $q_0 = (2, 3, 4)$, respectively. The bottom panels from left to right are for $q_0 = (2, 3, 4)$, respectively, with lines blue, red, and green corresponding to $\hat{\Pi}_0 = (5.0, 7.5, 10.0)$, respectively.

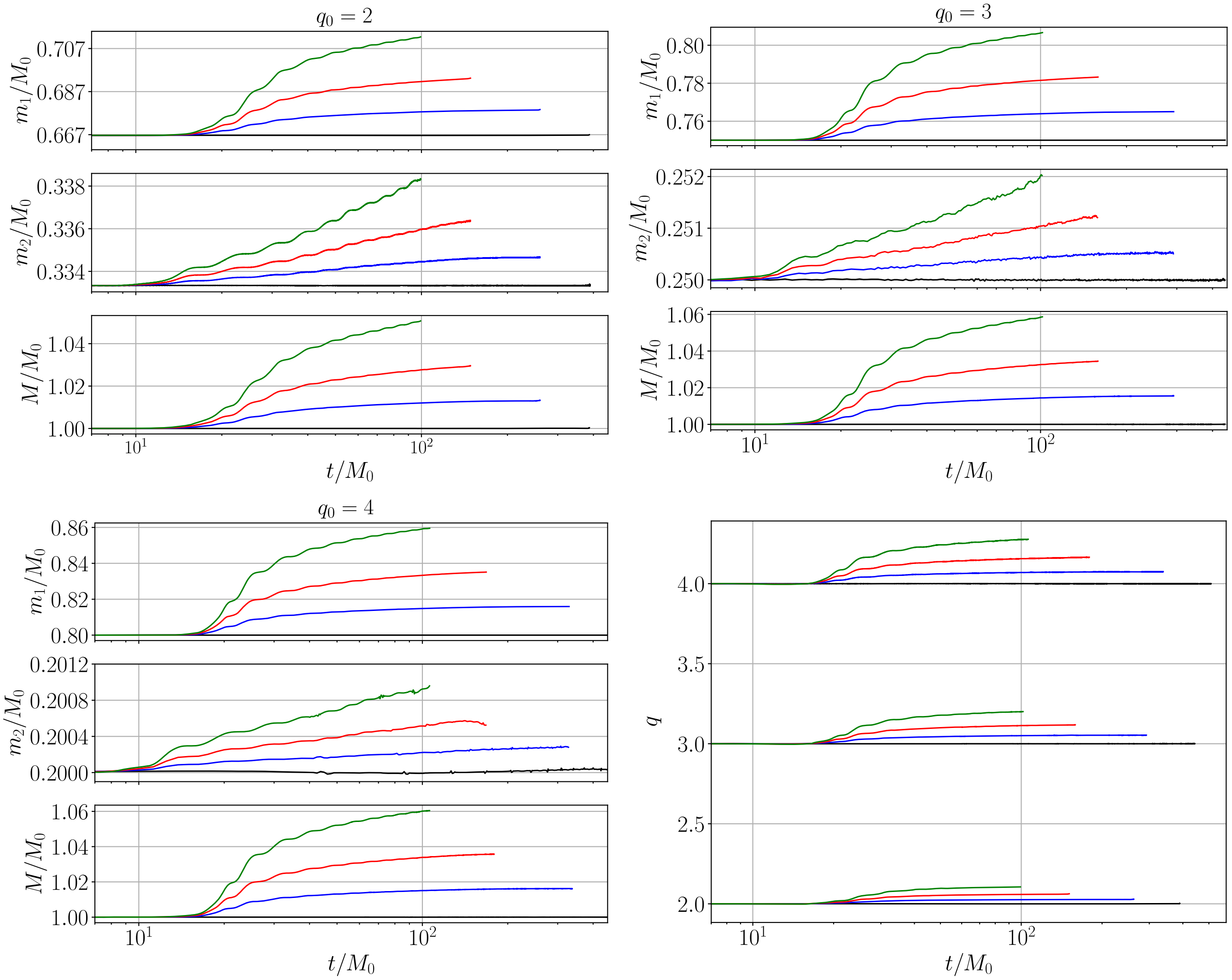

FIG. 3. Unequal mass, nonspinning BBHs: evolution of the BH masses m_1 and m_2, the total mass M, and the mass ratio q due to scalar field accretion. The black, red, blue, and green correspond to $\hat{\Pi}_0 = (0, 5.0, 7.5, 10.0)$, respectively. The lines end at the time when the merger occurs.

VI. UNEQUAL MASS, NONSPINNING BH BINARIES

Figure 2 shows the mode $l = 2$, $m = 2$ of the Weyl scalar Ψ_4 for the unequal mass and nonspinning BH binaries. The top panels from left to right are for $\hat{\Pi}_0 = (5.0, 7.5, 10.0)$, respectively, with lines blue, red, and green corresponding to $q_0 = (2, 3, 4)$, respectively. The bottom panels from left to right are for $q_0 = (2, 3, 4)$, respectively, with lines blue, red, and green corresponding to $\hat{\Pi}_0 = (5.0, 7.5, 10.0)$, respectively. From the top panels we see that, for a given $\hat{\Pi}_0$, the binary merges earlier for smaller q_0, as expected from the vacuum case, since the luminosity in GW during the inspiral scales as $q^2/(1+q)^4$ [27]. At the same time, for a given q_0, the larger the given value of $\hat{\Pi}_0$ is, the smaller the difference among the merger times.

From the bottom panels in Fig. 2, one sees that for a given q_0, the larger $\hat{\Pi}_0$, the earlier the binary merges. This is because the luminosity in GW also depends on the total mass of the binary M as M^2 [27]. As we shall see next, M grows monotonically with $\hat{\Pi}_0$. Also, when one slices the data this way, we observe that the differences with $\hat{\Pi}_0$ in merger times remain roughly the same independently of q_0.

The accretion of the scalar field by the BHs modifies the total binary mass M and its mass ratio q as it evolves. Figure 3 shows the evolution of m_1, m_2, and M for each initial q_0. As expected, accretion starts when the scalar field shell reaches the BHs, approximately at a time $\sim r_0$. The bottom right panel also shows the evolution of q due to the changes of the BH masses. In all panels, lines terminate at the time when the binary mergers, as signaled by the appearance of a common apparent horizon. The colors black, blue, red and green

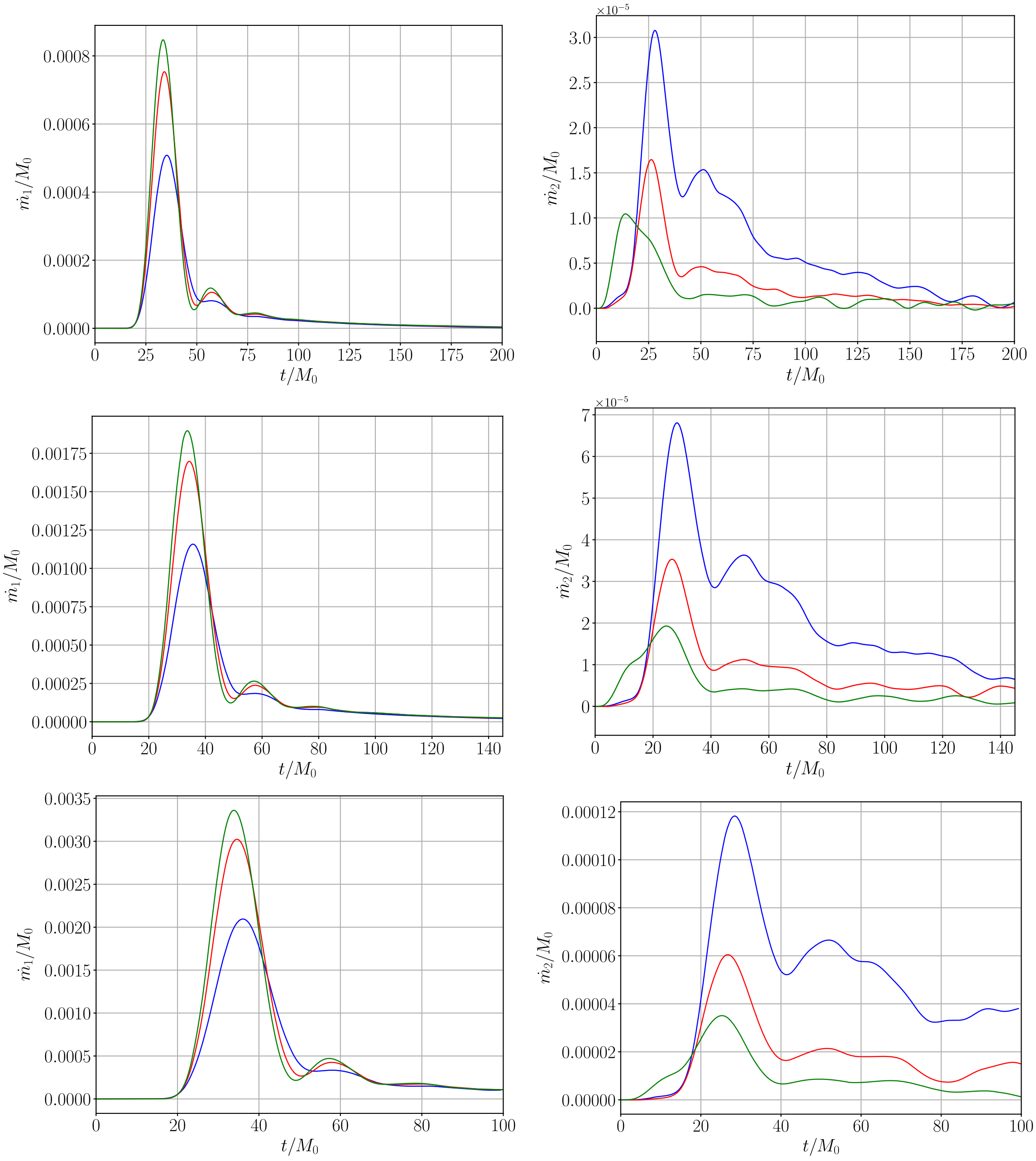

FIG. 4. Unequal mass, nonspinning BBH: mass accretion rates for each BH, top to bottom panels $\hat{\Pi}_0 = (0, 5.0, 7.5, 10.0)$, blue, red, and green correspond to $q_0 = (2, 3, 4)$, respectively.

denote $\hat{\Pi}_0 = (0, 5.0, 7.5, 10.0)$, respectively. Figure 4 shows the corresponding BH accretion rates.

From Figs. 3 and 4, we observe that the BH masses and accretion rates grow monotonically with $\hat{\Pi}_0$ for a given initial q_0. Furthermore, the growth is such that the increase in q is also monotonic with $\hat{\Pi}_0$. From Fig. 4, given a value of $\hat{\Pi}_0$, $\dot{m}_1 > \dot{m}_2$, similar to Bondi accretion behavior in which the accretion rate is proportional to the mass of the accreting object. By taking into consideration the growth in q observed in Fig. 3, namely $\dot{q} > 0$, one obtains that $\dot{m}_1 > q\dot{m}_2$.

Figure 5 shows the energy, angular momentum, and linear momentum radiated in GWs (dashed lines) and in the scalar field (solid lines) for the case $\hat{\Pi}_0 = 10.0$. We observe in the left panel that the energy radiated by the scalar field is higher than in GWs. This can be explained as follows: the ADM energy at the end of the simulations is given by $E_{\rm ADM} = E^{\rm rad}_{\rm GW} + E^{\rm rad}_{\phi} + m_f$, with m_f the mass of the final BH. For the case $q_0 = 2$ and $\hat{\Pi}_0 = 10.0$, we have from Table I that $E_{\rm ADM} = 1.102M_0$ and from Table III that $m_f = 1.0147M_0$; thus, $E^{\rm rad}_{\rm GW} + E^{\rm rad}_{\phi} = E_{\rm ADM} - m_f \simeq 0.087M_0$. Since energy

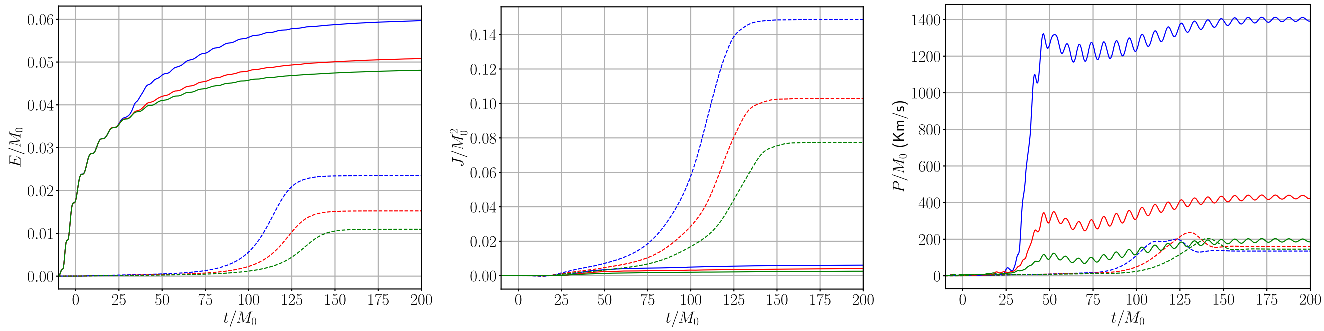

FIG. 5. Unequal mass, nonspinning BBH: energy, angular momentum, and linear momentum radiated in GWs (dashed lines) and in the scalar field (solid lines) for the case $\hat{\Pi}_0 = 10.0$. Colors blue, red, and green correspond to $q_0 = (2, 3, 4)$, respectively.

radiated in GWs is typically a few percent, in this case $E_{\rm GW} \simeq 0.025 M_0$, we have that $E_\phi^{\rm rad} \simeq 0.06 M_0$, consistent with the value in Fig. 5. Another characteristic in this figure is that, as with GWs, the energy radiated in the scalar field decreases monotonically with q_0.

The angular momentum radiated is depicted in the middle panel of Fig. 5. As expected, GWs carry away angular momentum and shrink the binary. The scalar field also extracts angular momentum but in smaller amounts. The reason why the scalar field angular momentum radiation is much smaller than the one in GWs is because initially the scalar field shell does not have any angular momentum. All the momentum generated is from the "stirring" of the scalar field by the binary.

The right panel in Fig. 5 shows the magnitude of linear momentum emitted, which for these nonprecessing binaries lies in the xy plane. As with the energy radiated, the emission of scalar field linear momentum is significantly larger than in the GWs. Also interesting is the oscillations in the scalar field linear momentum radiated, which are also observed in the energy and angular momentum but at a much smaller scale. The reason for this is because in systems of BBH with massive scalar fields, as it is in our case, the scalar fields develop long-lived modes due to the presence of an effective potential.

Table III shows the mass m_f, spin a_f, and kick velocity $v_{\rm kick}$ of the remnant BH, where we have combined the emission of linear momentum by GWs and the scalar field to estimate the gravitational recoil. Independently of q_0, m_f grows monotonically with $\hat{\Pi}_0$. This is expected from the way the BHs accrete the scalar field, namely, the more massive the hole, the more it accretes.

Regarding the final spin, we found that for a given $\hat{\Pi}_0$, a_f decreases as q_0 increases. Which is the same trend observed in the vacuum case; that is, the scalar field modifies the spin magnitude but not its dependence with q. On the other hand, if one fixes the attention to the final spin for a given q_0, one sees monotonicity in the $q_0 = 3$ and 4, decreasing its value with $\hat{\Pi}_0$ increasing. At first look, this seems counterintuitive because one would think that, since the larger the value of $\hat{\Pi}_0$, the earlier the binary merger, there would be a larger residual of angular momentum that goes into the final spin. Yes, there is more angular momentum in the final BH, but one has to also remember that $a_f = S_f/m_f^2$ is the dimensionless spin parameter, not the angular momentum S_f. It is the growth in the final mass of the BH responsible for the decrease in a_f. Since the growth in the masses for $q_0 = 2$ is not as large (see Fig. 3), the monotonicity of a_f with $\hat{\Pi}_0$ only shows for large values.

For the kick velocity, given a value of q_0, the recoil is larger than in the vacuum case and increases monotonically with $\hat{\Pi}_0$. In vacuum, the maximum kick velocity of the final BH in nonspinning, unequal-mass BBH occurs near $q_0 = 3$ [3]. In the presence of scalar field, we observe that the maximum kick for a given $\hat{\Pi}_0$ occurs for $q_0 \leq 2$, with $\hat{\Pi}_0 = 10.0$ reaching superkick levels. For a given $\hat{\Pi}_0$, all the kicks are larger than in the vacuum case, the reason for this is because in these configurations the emission of linear momentum is larger through the scalar field channel. The initial momentum in the scalar field is not directly

TABLE III. Mass m_f, spin a_f and kick of the final BH for the unequal mass, nonspinning BBH.

Case	m_f/M_0	a_f	$v_{\rm kick}$ (km/s)
q2-000	0.9612	0.6232	146
q2-050	0.9743	0.6218	550
q2-075	0.9893	0.6230	946
q2-100	1.0147	0.6267	1303
q3-000	0.9712	0.5405	166
q3-050	0.9869	0.5378	289
q3-075	1.0055	0.5370	409
q3-100	1.0337	0.5355	543
q4-000	0.9777	0.4713	149
q4-050	0.9942	0.4686	202
q4-075	1.0137	0.4646	256
q4-100	1.0422	0.4624	304

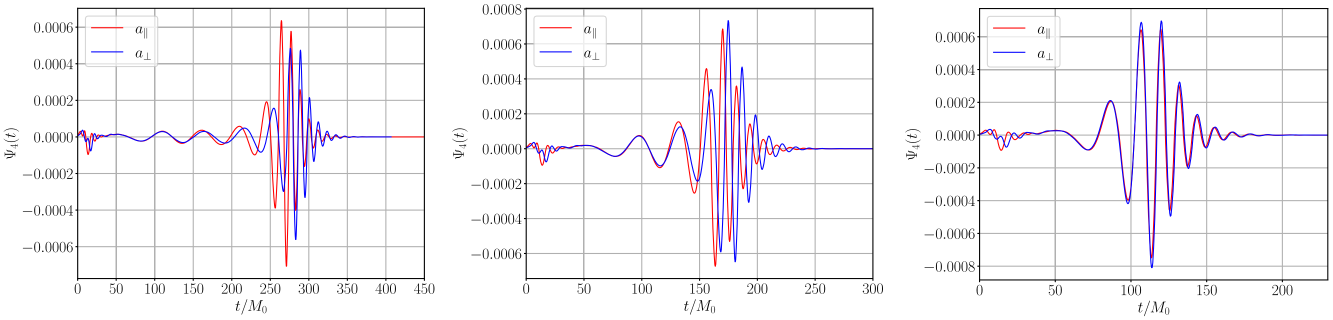

FIG. 6. Mode $l = 2$, $m = 2$ of the Weyl scalar Ψ_4 for the equal mass, spinning BH binaries. Panels from left to right correspond to $\hat{\Pi}_0 = (5.0, 7.5, 10.0)$, respectively, with red lines for $a_\parallel$ and blue for $a_\perp$.

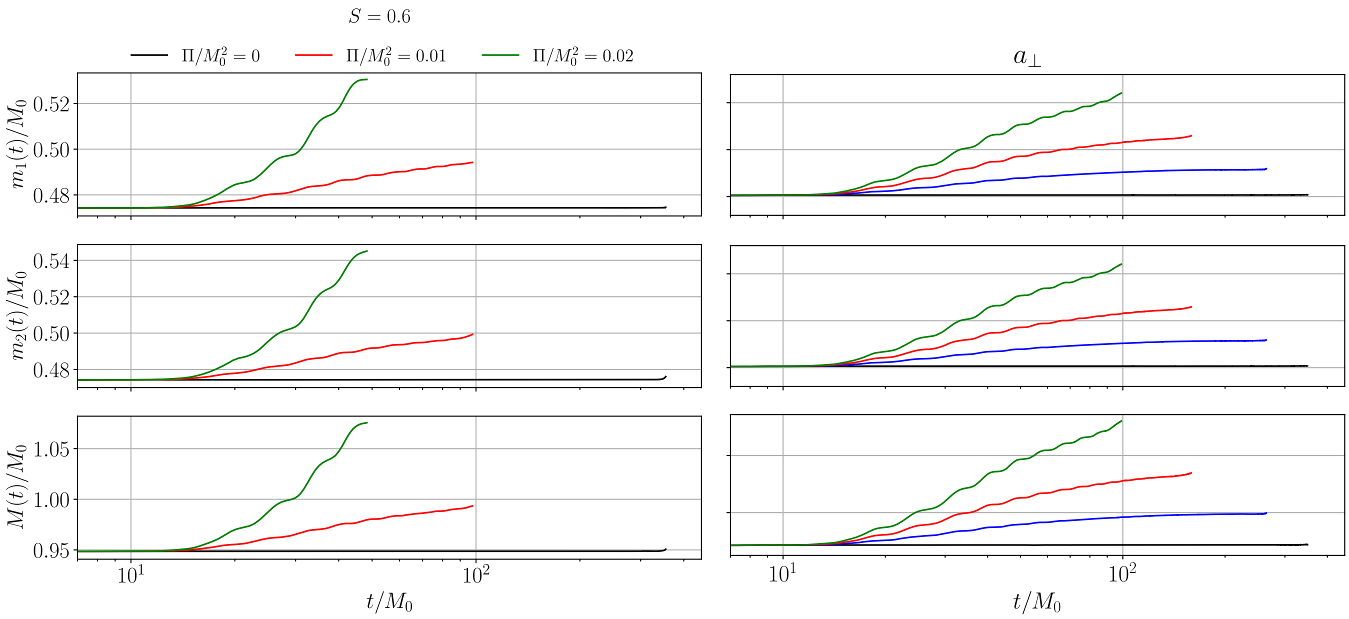

FIG. 7. Evolution of m_1, m_2 and M for equal mass, spinning BH binaries cases: left panel for $a_\parallel$ and right panel $a_\perp$. The colors black, blue, and green correspond to the scalar shell clouds with $\hat{\Pi}_0 = (0, 5.0, 7.5, 10.0)$ respectively. The lines end at the time when the merger occurs.

responsible for this since it does not have net linear momentum; it is spherically symmetric. It is through the interactions with the binary that linear momentum in the scalar field is redistributed and emitted in a particular direction. It turns out that this direction is aligned with that of the linear momentum emitted in GWs. To check the robustness of our kick velocity results, in addition to the convergence test presented in Sec. II, we used the heuristic formula (1) in [26] to compare our kick velocity calculations. We found that the values obtained for the vacuum cases q2-000, q3-000, and q4-000 are approximately 6.0%, 4.5%, and 4.6% different from those obtained with the formula.

VII. EQUAL MASS, SPINNING BH BINARIES

As mentioned before, we considered two setups for binaries with equal mass and antialigned spinning BHs. The $a_\parallel$ cases have BH spins along the direction of the orbital angular momentum (i.e., nonprecessing binaries), and the $a_\perp$ cases have BH spins in the orbital plane in the superkick configuration [25,26].

Figure 6 shows the mode $l = 2$, $m = 2$ of the Weyl scalar Ψ_4. Panels from left to right are for $\hat{\Pi}_0 = (5.0, 7.5, 10.0)$, respectively, with red lines for $a_\parallel$ and blue for $a_\perp$. It is interesting to notice that for $\hat{\Pi}_0 = 10.0$ there is very little difference in the (2, 2) mode between the $a_\parallel$ and $a_\perp$ case, this in spite of the large difference they have, as we shall see, in kicks produced. After all, the $a_\perp$ cases are in the superkick class. This means that the differences are in the higher modes. We also observe from the waveforms in Fig. 6 that, as for the unequal mass and nonspinning BH binaries, the larger the value of $\hat{\Pi}_0$, the earlier the binary merges, and the reasons are similar. The accretion of scalar

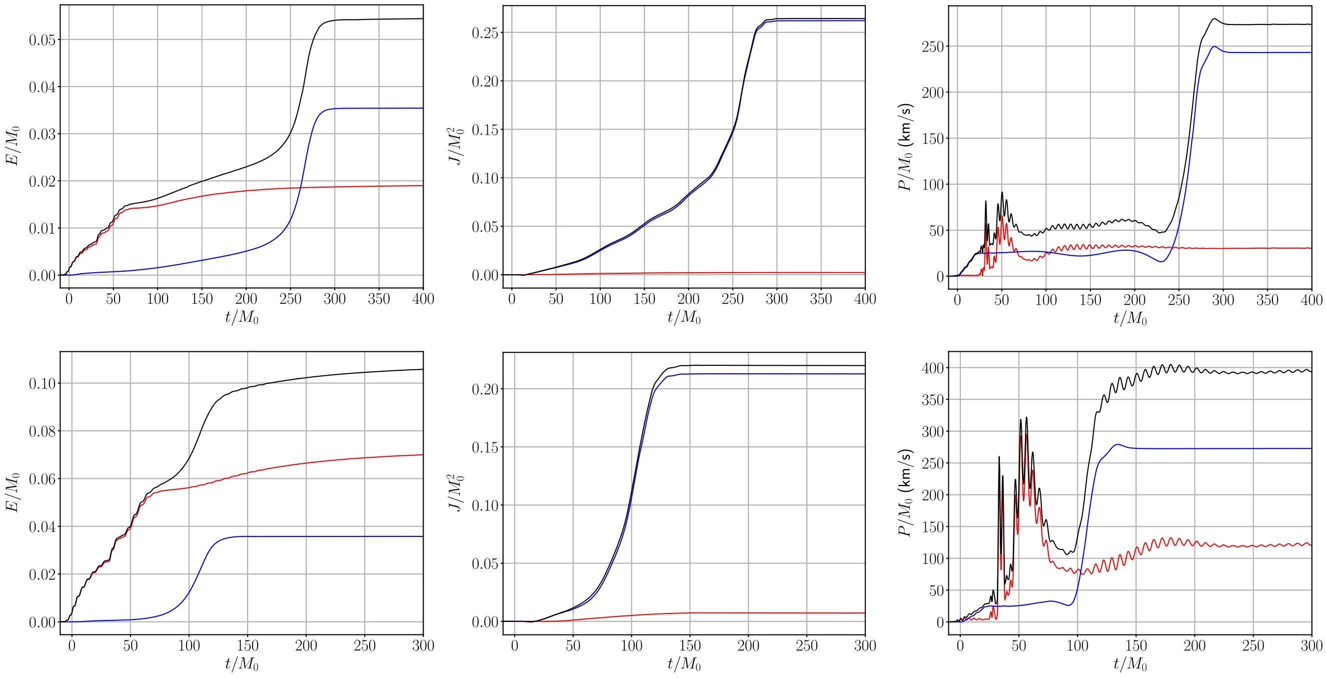

FIG. 8. Energy (left panels), angular momentum (middle panels), and linear momentum (right panels) radiated as a function of time in GWs (blue lines), in the scalar field (red lines), and the total (black lines) for the $a_{\|}$ cases, with the top panels for $\hat{\Pi}_0 = 5.0$ and the bottom panels for $\hat{\Pi}_0 = 10.0$.

field by the BH increases their masses and thus the luminosity of the binary.

Figure 7 shows from top to bottom the evolution of m_1, m_2, and M, respectively. The left panels are for the $a_{\|}$ cases and the right ones for $a_{\perp}$. The line colors black, blue, red, and green correspond to $\hat{\Pi}_0 = (0, 5.0, 7.5, 10.0)$, respectively. The behavior in the growth of the masses is similar to that of unequal mass, nonspinning BH binaries. Namely, the growth is monotonic with $\hat{\Pi}_0$. It is interesting to point out that the growth in m_1 and m_2 is identical in the $a_{\perp}$; thus, q remains unity. This is because, for both holes, the orientation of their spins relative to the orbital angular momentum is identical. On the other hand, since for the $a_{\|}$ cases the BH with mass m_1 has its spin aligned with the orbital angular momentum and for the other antialigned, it is clear from panels top left and middle left that there is a slight difference in the growth between hole m_1 and m_2. The BH with mass m_2 grows slightly more than m_1. This translates into mass ratios at merger of $q = 1.0049$, 1.0073, 1.0102 for $\hat{\Pi}_0 = 5.0$, 7.5, 10, respectively. This is consistent with accretion of spinning black holes immersed in a gaseous environment or circumbinary disks [49].

TABLE IV. Mass m_f, spin a_f and magnitude of the kick of the final BH for equal mass, spinning BBHs in the $a_{\|}$ cases.

Case	m_f/M_0	a_f	$\lvert v\rvert$ (km/s)
$a_{\|}000$	0.9512	0.6851	302
$a_{\|}050$	0.9603	0.6856	285
$a_{\|}075$	0.9691	0.6844	297
$a_{\|}100$	0.9850	0.6970	362

Figure 8 shows the energy, angular momentum, and linear momentum radiated as a function of time in GWs (blue lines), in the scalar field (red lines), and the total (black lines) for the $a_{\|}$ cases, with the top panels for $\hat{\Pi}_0 = 5.0$ and the bottom panels for $\hat{\Pi}_0 = 10.0$. We observe that the angular and linear momentum radiated in GWs is larger than in the scalar field for both $\hat{\Pi}_0$ values. This is not the case for the energy radiated. Not surprisingly, the larger the value of $\hat{\Pi}_0$, i.e. the larger the initial energy in the scalar field, the larger the energy emission. This does not imply that the remnant BH will have a smaller mass. As we can see from Table IV and saw from Fig. 7, the larger $\hat{\Pi}_0$, the larger the final BH because of the accretion of scalar field.

Regarding the radiated angular momentum from the middle panels of Fig. 8, the scalar field emission is significantly smaller than from GWs. However, when comparing the emission in GWs from $\hat{\Pi}_0 = 5.0$ (top-middle panel) with that of $\hat{\Pi}_0 = 10.0$ (bottom-middle panel), the former is slightly larger. Since the initial configuration has mostly orbital angular momentum because the spins are antialigned, this implies that the spin of the final BH for $\hat{\Pi}_0 = 5.0$ will be smaller than for $\hat{\Pi}_0 = 10.0$, as we can see in Table IV. This is consistent because the $\hat{\Pi}_0 = 10.0$ binary merges earlier (see Fig. 6),

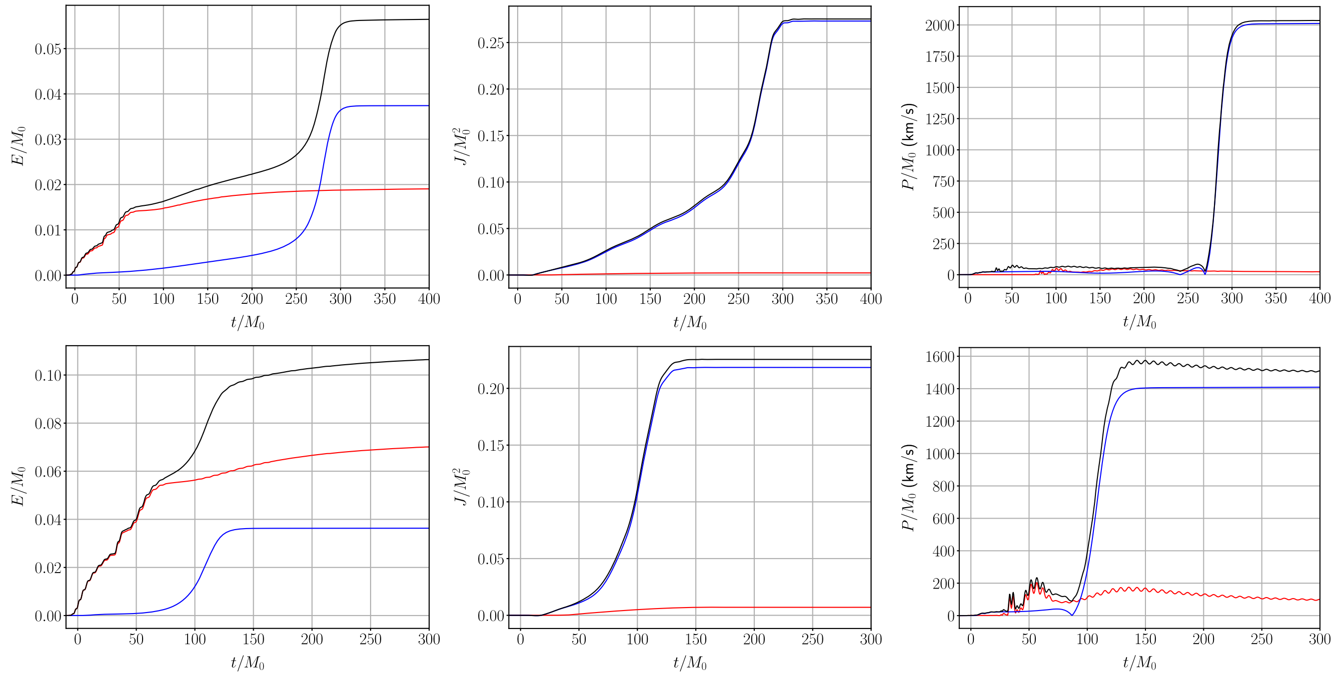

FIG. 9. Energy (left panels), angular momentum (middle panels), and linear momentum (right panels) radiated as a function of time in GWs (blue lines), in the scalar field (red lines), and the total (black lines) for the $a_\perp$ cases, with the top panels for $\hat{\Pi}_0 = 5.0$ and the bottom panels for $\hat{\Pi}_0 = 10.0$.

and thus it does not radiate as much angular momentum as with the $\hat{\Pi}_0 = 5.0$ case.

The situation seems to reverse with the linear momentum radiated. Similar to the angular momentum radiated, it is still the case that, as the binary merges earlier because of the presence of the scalar field, it does not "accumulate" as much kick as in the vacuum case (see kick values for $a_\parallel$050 and $a_\parallel$075 in Table IV). However, as we can see from the right panels in Fig. 8, the kick contribution from the scalar field increases with $\hat{\Pi}_0$ and eventually turns things around. At $\hat{\Pi}_0 = 10.0$ this contribution is such that the kick becomes larger than in the vacuum case.

Figure 9 shows the energy, angular momentum, and linear momentum radiated as a function of time in GWs (blue lines), in the scalar field (red lines), and the total (black lines) for the $a_\perp$ cases, with the top panels for $\hat{\Pi}_0 = 5.0$ and the bottom panels for $\hat{\Pi}_0 = 10.0$. It is interesting to observe that the spin configuration does not have a big effect on the energy and angular momentum radiated. The left and middle panels in Fig. 9 are very similar to those in Fig. 8 for the $a_\parallel$ cases. The differences come in the linear momentum radiated (right panels in Fig. 9). Although the trend of which radiation dominates is similar to those in the $a_\parallel$ cases, the magnitude of the emission in the $a_\perp$ cases is much larger, after all these are superkick setups.

Table V shows the mass, spin, and the z-component kick velocity (the most dominant in this cases) for the $a_\perp$ cases. Regarding the mass of the final BH, for the same reasons as all the previous binary types, m_f increases monotonically with $\hat{\Pi}_0$. There seems to be also monotonicity with $\hat{\Pi}_0$ in a_f. The reason is because the larger the value of $\hat{\Pi}_0$, the faster the binary merges thus the lower the angular momentum radiated and the larger residual angular momentum that goes into the final spin.

There is no monotonicity in the kicks. To help understand the situation, we plot the kicks as a function of $\hat{\Pi}_0$ in Fig. 10. In this figure, we observe hints of an oscillatory trend in the z component of the kick as a function of $\hat{\Pi}_0$. The reason for this oscillatory behavior is similar to the one found in the first studies of superkicks, namely that the magnitude and direction of the kick is proportional to the cosine of the angle that the in-plane components of

TABLE V. Mass m_f, spin a_f and z component of the kick of the final BH for equal mass, spinning BBHs in the $a_\perp$ cases.

Case	m_f/M_0	a_f	v_z (km/s)
$a_\perp$0000	0.9500	0.6797	−2113
$a_\perp$0125	0.9500	0.6786	−2138
$a_\perp$0250	0.9515	0.6801	−1422
$a_\perp$0375	0.9560	0.6860	1020
$a_\perp$0500	0.9582	0.6802	2113
$a_\perp$0625	0.9650	0.6834	−1281
$a_\perp$0750	0.9691	0.6829	335
$a_\perp$0875	0.9734	0.6848	1669
$a_\perp$1000	0.9841	0.6966	−1576

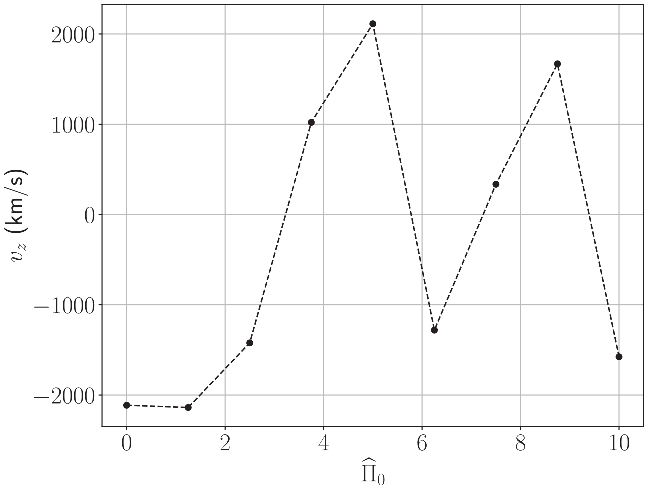

FIG. 10. Final kick as a function of $\hat{\Pi}_0$ for the $a_\perp$ (superkick setup) values in Table V.

the spins make with the infall direction at merger [50]. In the vacuum case, this dependence is obtained by changing the initial direction of the spins. In our case, it is the effect that the scalar field has on the mass growth of the holes, and thus its orbital dynamics, that produces the changes of the spin alignment relative to the infall direction. Similar to what we did in Sec. VI, we used the heuristic formula from [26] to compare our kick velocity calculations. We found that there is an approximately 6% difference for the case $a_\parallel$000 and 7% for the case $a_\perp$0000 between our results and those from the heuristic formula.

VIII. CONCLUSIONS

We have presented results from a numerical study of BBH mergers immersed in a scalar field cloud, focusing on the effects that the cloud has on the gravitational recoil, as well as on the spin of the final BH. We considered two initial configuration scenarios: binaries with nonspinning, unequal mass BHs and binaries with equal mass BHs and their spins antialigned. For the later case we had two subcategories, one in which the BH spins were parallel to the orbital angular momentum (i.e. nonprecessing), and the other with the BH spins in the orbital plane in the so-called superkick setup. The initial geometry of the scalar field cloud was a thin shell encapsulating the binary.

In all cases, because of scalar field accretion, the BHs gained mass, thus increased the emission of GWs, and as a consequence accelerated the merger. This also induced changes in the mass ratio of the binary, with the exception of the binaries in the superkick configuration because the spins relative to the orbital momentum were the same.

We computed the radiated energy, angular momentum, and linear momentum emitted in both the GW and scalar field channels. For the unequal mass BH binaries, we found that the scalar field emission was dominant in energy and linear momentum. Because of the later, the kicks were larger than in the vacuum case. Since the emission of angular momentum by the scalar field was smaller than from GWs, the spins varied very little from their vacuum counterparts. A similar situation took place with the equal mass, spinning BH binaries; the presence of the scalar field did not translate into significant changes in the spin of the final BH relative to the vacuum case. The main reason for this general situation is because the initial scalar field cloud did not have angular momentum that could be transferred via accretion to the BHs.

Regarding the gravitational recoil of the final BH, for the case of unequal mass, nonspinning BH binaries, we obtained that the kicks were larger than their vacuum counterparts because in these configurations the emission of linear momentum is larger via the scalar field channel. Some of the kicks reached superkick levels of ∼1, 300 km/s.

For the binaries with equal mass BHs and spins aligned with the orbital angular momentum, we observed two effects competing against each other as we increased $\hat{\Pi}_0$. The scalar field accretion increased the BH masses and accelerated the merger. This ameliorated the “accumulation” of the kick. Acting in the opposite direction was the linear momentum radiated in the scalar field, increasing with the value of $\hat{\Pi}_0$ and eventually yielding kicks larger than in the vacuum case.

Finally, for equal mass and spinning BH binaries in the superkick configuration, we observed hints of the oscillatory behavior observed in the vacuum case. The reasons are similar; that is, the magnitude and direction of the kick is proportional to the cosine of the angle that the in-plane components of the spins make with the infall direction at merger [50]. However, instead of this dependence from changing the initial direction of the spins, in our case, it is the change in the dynamics of the binary from the mass growth of the holes that produces the changes of the spin alignment relative to the infall direction.

One, of course, must take our results with a grain of salt regarding astrophysical implications. The purpose of our study was solely to investigate the sensitivity of BBH merger dynamics and the resulting final BH to the presence of a scalar field. Our results should be taken as a guide of the scale of energy in a scalar field necessary to imprint noticeably effects on the merger time of the binary and the gravitational recoil of the final black hole. In a subsequent study, we will focus on the impact in parameter estimation under the eyepiece of GW analysis.

ACKNOWLEDGMENTS

This work was supported in part by NSF Awards No. 2207780 and No. 2114582 to P. L. and D. S., the National Key Research and Development Program of China (Grant No. 2020YFC2201503), the National Natural Science Foundation of China (Grants

No. 12105126, No. 11875151, No. 11705070, No. 12075103, and No. 12047501), the China Postdoctoral Science Foundation (Grant No. 2021M 701531), the 111 Project under (Grant No. B20063), and the Fundamental Research Funds for the Central Universities (Grant No. lzujbky-2021-pd08).

---

[1] Milton Ruiz, Miguel Alcubierre, Darío Núñez, and Ryoji Takahashi, Multiple expansions for energy and momenta carried by gravitational waves, Gen. Relativ. Gravit., **40**, 1705 (2007).

[2] M. J. Fitchett, The influence of gravitational wave momentum losses on the centre of mass motion of a Newtonian binary system, Mon. Not. R. Astron. Soc. **203**, 1049 (1983).

[3] José A. González, Ulrich Sperhake, Bernd Brügmann, Mark Hannam, and Sascha Husa, Maximum Kick from Nonspinning Black-Hole Binary Inspiral, Phys. Rev. Lett. **98**, 091101 (2007).

[4] James Healy, Frank Herrmann, Ian Hinder, Deirdre M. Shoemaker, Pablo Laguna, and Richard A. Matzner, Superkicks in Hyperbolic Encounters of Binary Black Holes, Phys. Rev. Lett. **102**, 041101 (2009).

[5] Carlos F. Sopuerta, Nicolás Yunes, and Pablo Laguna, Gravitational recoil velocities from eccentric binary black hole mergers, Astrophys. J. Lett. **656**, L9 (2007).

[6] Bhavesh Khamesra, Miguel Gracia-Linares, and Pablo Laguna, Black hole-neutron star binary mergers: The imprint of tidal deformations and debris, Classical Quantum Gravity **38**, 185008 (2021).

[7] David J. E. Marsh, Axion cosmology, Phys. Rep. **643**, 1 (2016).

[8] Fedor Bezrukov and Mikhail Shaposhnikov, The standard model Higgs boson as the inflaton, Phys. Lett. B **659**, 703 (2008).

[9] C. P. Burgess, Hyun Min Lee, and Michael Trott, Power-counting and the validity of the classical approximation during inflation, J. High Energy Phys. 09 (2009) 103.

[10] C. P. Burgess, Hyun Min Lee, and Michael Trott, Comment on Higgs inflation and naturalness, J. High Energy Phys. 07 (2010) 007.

[11] Gian F. Giudice and Hyun Min Lee, Unitarizing Higgs inflation, Phys. Lett. B **694**, 294 (2011).

[12] Rose N. Lerner and John McDonald, Higgs inflation and naturalness, J. Cosmol. Astropart. Phys. 04 (2010) 015.

[13] David H. Lyth and Antonio Riotto, Particle physics models of inflation and the cosmological density perturbation, Phys. Rep. **314**, 1 (1999).

[14] Robert V. Wagoner, Scalar tensor theory and gravitational waves, Phys. Rev. D **1**, 3209 (1970).

[15] Antonio De Felice and Shinji Tsujikawa, f(R) theories, Living Rev. Relativity **13**, 3 (2010).

[16] Thomas P. Sotiriou and Valerio Faraoni, $f(R)$ theories of gravity, Rev. Mod. Phys. **82**, 451 (2010).

[17] Eloisa Bentivegna, Deirdre M. Shoemaker, Ian Hinder, and Frank Herrmann, Probing the binary black hole merger regime with scalar perturbations, Phys. Rev. D **77**, 124016 (2008).

[18] James Healy, Tanja Bode, Roland Haas, Enrique Pazos, Pablo Laguna, Deirdre M. Shoemaker, and Nicolás Yunes, Late inspiral and merger of binary black holes in scalar-tensor theories of gravity, Classical Quantum Gravity **29**, 232002 (2012).

[19] Emanuele Berti, Vitor Cardoso, Leonardo Gualtieri, Michael Horbatsch, and Ulrich Sperhake, Numerical simulations of single and binary black holes in scalar-tensor theories: Circumventing the no-hair theorem, Phys. Rev. D **87**, 124020 (2013).

[20] Zhoujian Cao, Pablo Galaviz, and Li-Fang Li, Binary black hole mergers in $f(R)$ theory, Phys. Rev. D **87**, 104029 (2013).

[21] Eric W. Hirschmann, Luis Lehner, Steven L. Liebling, and Carlos Palenzuela, Black hole dynamics in Einstein-Maxwell-dilaton theory, Phys. Rev. D **97**, 064032 (2018).

[22] Maria Okounkova, Leo C. Stein, Mark A. Scheel, and Daniel A. Hemberger, Numerical binary black hole mergers in dynamical Chern-Simons gravity: Scalar field, Phys. Rev. D **96**, 044020 (2017).

[23] Qing Yang, Li-Wei Ji, Bin Hu, Zhou-Jian Cao, and Rong-Gen Cai, An axion-like scalar field environment effect on binary black hole merger, Res. Astron. Astrophys. **18**, 065 (2018).

[24] Helvi Witek, Leonardo Gualtieri, Paolo Pani, and Thomas P. Sotiriou, Black holes and binary mergers in scalar Gauss-Bonnet gravity: Scalar field dynamics, Phys. Rev. D **99**, 064035 (2019).

[25] José A. González, Mark Hannam, Ulrich Sperhake, Bernd Brügmann, and Sascha Husa, Supermassive Recoil Velocities for Binary Black-Hole Mergers with Antialigned Spins, Phys. Rev. Lett. **98**, 231101 (2007).

[26] Manuela Campanelli, Carlos O. Lousto, Yosef Zlochower, and David Merritt, Maximum Gravitational Recoil, Phys. Rev. Lett. **98**, 231102 (2007).

[27] Thomas W. Baumgarte and Stuart L. Shapiro, *Numerical Relativity: Solving Einstein's Equations on the Computer* (Cambridge University Press, Cambridge, England, 2010).

[28] A. Lichnerowicz, L'integration des équations relativistes et le problème des n corps, J. Math. Pures Appl. **23**, 37 (1944).

[29] James W. York, Gravitational Degrees of Freedom and the Initial-Value Problem, Phys. Rev. Lett. **26**, 1656 (1971).

[30] James W. York, Role of Conformal Three-Geometry in the Dynamics of Gravitation, Phys. Rev. Lett. **28**, 1082 (1972).

[31] Gregory B. Cook, Initial data for numerical relativity, Living Rev. Relativity **3**, 5 (2000).

[32] Pablo Laguna, Hannu Kurki-Suonio, and Richard A. Matzner, Inhomogeneous inflation: The initial-value problem, Phys. Rev. D **44**, 3077 (1991).

[33] Jayashree Balakrishna, Ruxandra Bondarescu, Gregory Daues, F. Siddhartha Guzman, and Edward Seidel, Evolution of 3-D boson stars with waveform extraction, Classical Quantum Gravity **23**, 2631 (2006).

[34] Jeffrey M. Bowen and James W. York, Time-asymmetric initial data for black holes and black-hole collisions, Phys. Rev. D **21**, 2047 (1980).

[35] Marcus Ansorg, Bernd Bruegmann, and Wolfgang Tichy, A single-domain spectral method for black hole puncture data, Phys. Rev. D **70**, 064011 (2004).

[36] Thomas W. Baumgarte and Stuart L. Shapiro, Numerical integration of Einstein's field equations, Phys. Rev. D **59**, 024007 (1998).

[37] Masaru Shibata and Takashi Nakamura, Evolution of three-dimensional gravitational waves: Harmonic slicing case, Phys. Rev. D **52**, 5428 (1995).

[38] Manuela Campanelli, C. O. Lousto, P. Marronetti, and Y. Zlochower, Accurate Evolutions of Orbiting Black-Hole Binaries Without Excision, Phys. Rev. Lett. **96**, 111101 (2006).

[39] John G. Baker, Joan Centrella, Dae-Il Choi, Michael Koppitz, and James van Meter, Gravitational Wave Extraction from an Inspiraling Configuration of Merging Black Holes, Phys. Rev. Lett. **96**, 111102 (2006).

[40] Tom Goodale, Gabrielle Allen, Gerd Lanfermann, Joan Masso, Thomas Radke, Edward Seidel, and John Shalf, The cactus framework and toolkit: Design and applications, in *VECPA Vector and Parallel Processing R'2002, 5th International Conference* (Springer, Berlin, 2003).

[41] Sascha Husa, Ian Hinder, and Christiane Lechner, Kranc: A *Mathematica* package to generate numerical codes for tensorial evolution equations, Comput. Phys. Commun. **174**, 983 (2006).

[42] Roland Haas, Roman V. Shcherbakov, Tanja Bode, and Pablo Laguna, Tidal disruptions of white dwarfs from ultra-close encounters with intermediate-mass spinning black holes, Astrophys. J. **749**, 117 (2012).

[43] Christopher Evans, Pablo Laguna, and Michael Eracleous, Ultra-close encounters of stars with massive black holes: Tidal disruption events with prompt hyperaccretion, Astrophys. J. Lett. **805**, L19 (2015).

[44] Michael Clark and Pablo Laguna, Bowen-York-type initial data for binaries with neutron stars, Phys. Rev. D **94**, 064058 (2016).

[45] Karan Jani, James Healy, James A. Clark, Lionel London, Pablo Laguna, and Deirdre Shoemaker, Georgia tech catalog of gravitational waveforms, Classical Quantum Gravity **33**, 204001 (2016).

[46] Steven R. Brandt *et al.*, The Einstein Toolkit, December 2021, http://einsteintoolkit.org.

[47] Abhay Ashtekar and Badri Krishnan, Isolated and dynamical horizons and their applications, Living Rev. Relativity **7**, 10 (2004).

[48] William E. East and Frans Pretorius, Superradiant Instability and Backreaction of Massive Vector Fields Around Kerr Black Holes, Phys. Rev. Lett. **119**, 041101 (2017).

[49] Federico G. Lopez Armengol, Luciano Combi, Manuela Campanelli, Scott C. Noble, Julian H. Krolik, Dennis B. Bowen, Mark J. Avara, Vassilios Mewes, and Hiroyuki Nakano, Circumbinary disk accretion into spinning black hole binaries, Astrophys. J. **913**, 16 (2021).

[50] Manuela Campanelli, Carlos Lousto, Yosef Zlochower, and David Merritt, Large merger recoils and spin flips from generic black hole binaries, Astrophys. J. **659**, L5 (2007).